Diffusion of CH_4 and N_2 in Barium-exchanged reduced pore zorite (Ba-RPZ) and Zeolite 4A

Nicholas Stiles Wilkins, James A. Sawada, and Arvind Rajendran*[a]

Department of Chemical and Materials Engineering, University of Alberta, 12th Floor,
Donadeo Innovation Centre for Engineering (ICE), 9211 - 116 Street, Edmonton, Alberta,
CANADA, T6G 1H9

E-mail: *arvind.rajendran@ualberta.ca

---

[a] Correspondence concerning this article should be addressed to A. Rajendran at this current address: Department of Chemical and Materials Engineering, University of Alberta, 12th Floor, Donadeo Innovation Centre for Engineering (ICE), 9211 - 116 Street, Edmonton, Alberta, CANADA, T6G 1H9

Abstract

Barium-exchanged reduced pore zorite (Ba-RPZ) is a titanosilicate molecular sieve that separates CH_4 from N_2 based on their relative molecular sizes. A detailed study of N_2 and CH_4 adsorption equilibrium and diffusion on Ba-RPZ was completed using low and high-pressure volumetry. Adsorption equilibrium data for Ba-RPZ from vacuum to 1.2 bar were measured at 30, 40, and 50°C for CH_4 and at 30, 50, and 70°C for N_2. Constant volume uptake experiments were conducted to estimate the diffusivities of CH_4 at 30, 40, and 50°C and N_2 at -20, -10, and 0°C. Similar experiments were carried out with zeolite 4A to validate the methods used in this study. On the one hand, the transport of N_2 in Ba-RPZ was found to be controlled by diffusion in the micropores. On the other hand, the transport of CH_4 in Ba-RPZ was described by a dual-resistance model, including a barrier resistance and micropore diffusional resistance. Both the barrier and micropore diffusion coefficients demonstrated concentration dependence. While the micropore diffusion constant followed Darken's relationship, the barrier resistance did not. The activation energies of the micropore diffusion and barrier resistance for CH_4 on Ba-RPZ were calculated to be 30.46 and 60.19 kJ/mol, while that of micropore diffusion for N_2 on Ba-RPZ was calculated to be 25.77 kJ/mol. A concentration-dependent dual-resistance diffusion model for methane was constructed and validated using experimental data across a range of pressures and temperatures. The concentration-dependent dual-resistance model was able to describe the complex diffusion behaviour methane displays as it progressed from the dual-resistance controlled region to the micropore-controlled region of the isotherm. The calculated limiting N_2/CH_4 kinetic selectivity of Ba-RPZ was shown to be $\approx$ three orders of magnitude larger than the current benchmark material for CH_4/N_2 separation (Sr-ETS-4).

Keywords: volumetry, diffusion, titanosilicate, Ba-RPZ, zeolite 4A, barrier resistance, methane upgrading

Introduction

Methane is considered a cleaner form of fossil fuel due to its high energy density and low CO_2 emissions compared to coal and oil. Considering the low CO_2 intensity and with the possibility of capturing CO_2 emissions, natural gas is considered as an important fuel that will enable the transition to a net-zero society. A significant amount of geologic methane remains stranded in wells which have concentrations of N_2 large enough for the gas to fail pipeline specifications (CH_4 purity > 96 mol%)[1]. Many of the contaminated wells are not of a scale suitable to take advantage of cryogenic distillation but would be able to take advantage of alternate technologies such as pressure swing adsorption (PSA)[1–3]. Most adsorbents show preferential adsorption of CH_4 over N_2. This means that CH_4 is typically obtained as the low-pressure raffinate product and has to be re-compressed to meet pipeline specifications. To allow methane to be produced as the desired raffinate product, a different type of adsorbent is required; one that can separate CH_4 and N_2 based on their relative molecular sizes. Since CH_4 is the larger of the two, a PSA incorporating a size-selective molecular sieve is capable of producing methane as the light product[4]. Such adsorbents are typically referred to as "kinetic" adsorbents because they separate gases based on the differences in diffusion rates into the molecular sieve. Many adsorbents have been proposed for the kinetic separation of CH_4 from N_2, such as carbon molecular sieves[3–5], zeolite 4A[6,7] and clinoptilolites[8,9].

Strontium exchanged Engelhard titanosilate-4 (Sr-ETS-4,), is used commercially to separate CH_4 and N_2. The pore size of Sr-ETS-4 can be tuned by carefully controlling the temperature to which it is heated[10]. Effective pore size control on the order of 0.1 Å has been shown, and by heating the adsorbent to a temperature of roughly 275°C, the effective pore size of the material contracted to a diameter near the molecular diameter of methane[11]. Ba-ETS-4 and Na-ETS-4 have also been studied for their potential for CH_4/N_2 separations[11,12]. Marathe *et al.* measured uptake curves and pore diffusional time constants for Sr-ETS-4 and Na-ETS-4 and determined the limiting mass transfer mechanism to be gas diffusion within the micropores[11,13]. Jayaraman *et al.* simulated a 5-step cycle with Sr-ETS-4 and found process conditions where CH_4 purities greater than 96 mol% were achieved from a feed of 85/15 mol% CH_4/N_2[8]. Majumdar *et al.* studied Ba-ETS-4 and determined the same limiting mass transfer mechanism as Na- and Sr-ETS-4[12]. Bhadra *et al.*. performed process studies of Ba-ETS-4 and Sr-ETS-4 using a simple Skarstrom cycle and were able to find operating conditions that could purify CH_4 above 96 mol% from a feed of 90/10 mol% CH_4/N_2[14].

Another titanosilicate adsorbent that is a potential candidate for the kinetic separation of CH_4/N_2 is Ba-RPZ (barium-exchanged reduced pore zorite)[15,16]. Reduced pore zorites are structurally analogous to ETS-4 (another synthetic zorite) but are synthesized in a mixture rich in halogen ions other than fluorine. The adsorptive characteristics of the resulting materials indicate that the effective pore size of the material decreases in proportion to the size of the anion present in the synthesis mixture. It has been proposed that the halogen ions can isomorphically substitute the terminal hydroxl group connected to the titania group, which protrudes into the pore channel[17]. In doing so, the substitution of Cl, Br, or I for the smaller hydroxyl species creates a diffusion barrier within the pore channel that allows the molecular sieve to separate gases based on their relative size[17].

Single component equilibrium data have been reported by in Lin *et al.* for N_2 and CH_4 on Ba-RPZ at an unspecified temperature from 1 mbar to 1 bar pressure[17]. In the Ba-RPZ patent by Sawada *et al.*, single-component isotherms for N_2 and CH_4 at 30°C from vacuum pressures to 50 bar are reported[16]. While the data is conclusive that the adsorbent has a substantial selectivity toward N_2, a more detailed adsorption study is required to compare Ba-RPZ with other molecular sieves and to probe the underlying diffusion mechanism. An accurate mathematical description of the dynamic adsorption behaviour of N_2 and CH_4 in Ba-RPZ would provide a key component to the design of a kinetic pressure swing adsorption separation process.

Materials and Methods

Ba-RPZ crystals were obtained from Extraordinary Adsorbents Inc. (Edmonton, Alberta, Canada). The crystalline Ba-RPZ powder (without binder) is composed of platelets having a crystalline thickness of 94 ± 17 nm and width of 1.079 ± 0.252 μm. The Ba-RPZ sample studied in this paper is most similar to the Ba-RPZ-1 sample that was studied by Lin *et al.*.[17]. The zeolite 4A sample is a crystalline powder and was provided by Arkema (NK 10 AP or "Siliporite"). The zeolite 4A sample has cubic crystalline dimensions of 2.81 ± 0.59 μm. The scanning electron microscopy (SEM) images used to estimate the particle sizes of Ba-RPZ and zeolite 4A are shown in the Supporting Information (Fig. S2). All gases in this study (99.99% CH_4, 99.999% N_2 and 99.999% Ar) were obtained from Praxair Canada. Single component adsorption isotherms and diffusion characteristics for N_2 and CH_4 were measured using volumetry.

Equilibrium Measurements

Low-pressure volumetric isotherms for N_2 and CH_4 were measured with a Micromeritics ASAP 2020C (Norcross, GA, USA). The Micromeritics system was used to measure adsorption equilibrium between 1 mbar to 1.2 bar. The system has a loading accuracy of 0.15% of the reading and pressure accuracy of 1.3×10^{-7} mbar. A sample mass of 339.3 mg (Ba-RPZ) or 212.8 mg (zeolite 4A) was used for these experiments. The saturation loadings of CH_4 and N_2 were determined using a high-pressure volumetry apparatus (HPVA) (VTI Instruments, Hialeah, FL). The HPVA was used to measure equilibrium data between 0.25 and 20 bar and has a pressure accuracy of < 0.1 bar. A sample mass of 625.5 mg (Ba-RPZ) was used for the high-pressure adsorption experiments. The sample chambers for both instruments were thermostated with a 60/40 vol% ethylene glycol/water mixture for the lower temperature (< 20°C) experiments and either a furnace or an oil bath for the higher temperature (> 20°C) experiments. Prior to each experiment, in both the low and high-pressure systems, Ba-RPZ and zeolite 4A were activated for 12 hours under vacuum (5 μbar) at 250°C (Ba-RPZ) or 350°C (zeolite 4A).

Kinetic Measurements

Adsorption uptake experiments were performed using the Rate of Adsorption (ROA) package in the Micromeritics ASAP 2020C (Norcross, GA, USA). The sample chamber was thermostated with an ethylene glycol/water mixture for the lower temperature experiments (< 20°C) and an oil bath at temperatures greater than 20°C. A sample mass of 155.8 mg (large doses) or 169.8 mg (small doses) for Ba-RPZ and 331.1 mg for zeolite 4A was used for these experiments. Uptake data was measured by activating the sample under vacuum at 250°C (Ba-RPZ) or 350°C (zeolite 4A) for 12 hours. After activation, a fixed amount of gas was introduced into the sample chamber, and the pressure was measured as a function of time until the pressure in the system was stable[18,19]. After equilibrium was reached, the next dose was applied, and the same sequence followed until a series of uptake experiments were completed for a given temperature. Small pressure steps were introduced to the chamber to ensure that the calculated diffusivities would be along the local gradient of the isotherm and hence could be considered to be constant[18]. The change in pressure between each constant volume experiment was $\approx$ 15 to 300 mbar. These pressure steps were achieved by dosing a fixed quantity of gas into the sample chamber for each successive dose.

Modeling

Adsorption Equilibria

The single-site Langmuir (SSL) isotherm was used to fit the collected equilibrium data in this study. The SSL isotherm is shown below:

$$q_i^* = \frac{q_{\mathrm{b},i}^{\mathrm{sat}} b_i p_i}{1 + b_i p_i} = \frac{K_i p_i}{1 + b_i p_i} \tag{1}$$

where $q_{\mathrm{b}}^{\mathrm{sat}}$ is the saturation capacity of the material. The equilibrium constant b_i is a function of temperature, T:

$$b_i = b_{0,i}\mathrm{exp}\left(\frac{-\Delta H_{\mathrm{ads},i}}{RT}\right) \tag{2}$$

and $\Delta H_{\mathrm{ads},i}$ is the heat of adsorption. The temperature dependent Henry constant, K_i, is the product of q^{sat} and b_i.

The collected equilibrium data was fit to either a linear or SSL isotherm, depending on the sorbate-sorbent pairs, by minimizing the sum of squared errors:

$$J_1 = \sum_{i=j}^{n}\left[q^*_{\mathrm{exp},j} - q^*_{\mathrm{model},j}\right]^2 \tag{3}$$

where $q^*_{\mathrm{exp},j}$ and $q^*_{\mathrm{model},j}$ denote the experimentally measured and fitted values, respectively. The isosteric heat of adsorption, ΔH_{iso}, was calculated using the Clausius-Clapeyron equation:

$$\left[\frac{\partial \mathrm{ln}(p_i)}{\partial(1/T)}\right]_{q_i^*} = -\frac{\Delta H_{\mathrm{iso},i}}{R} \tag{4}$$

The derivative in Eqn. 4 was evaluated numerically using the collected equilibrium data at a fixed value of q_i^*. If a value of q_i^* did not exist for a particular temperature, it was determined through a linear interpolation.

Adsorption Kinetics

The transient mass uptake can be represented as a dimensionless fractional uptake:

$$\frac{m_t}{m_\infty} = \frac{\bar{q}(t) - q(0)}{q(\infty) - q(0)} \tag{5}$$

where $\bar{q}(t)$ is the average concentration (or loading) in the solid phase at time t, $q(0)$ is the initial solid phase concentration and $q(\infty)$ is the solid phase concentration after equilibrium has been achieved[20]. Experimentally, the constant volume apparatus measures the change in pressure during the experiment and then calculates the loadings. If the main mass transfer resistance is not from the macro or mesopores, the mass uptake profiles can be modeled with one of three micropore diffusion models[18,21,22].

Micropore Controlled: The first mechanism considers the primary mass transfer resistance to be transport within the micropores. The mass balance inside the micropore of a spherical crystalline particle is:

$$\frac{\partial q}{\partial t} = \frac{1}{r^2}\frac{\partial}{\partial r}\left(r^2 D_\mathrm{c}\frac{\partial q}{\partial r}\right) \tag{6}$$

where r is the radius at some point inside the crystal and D_c is the microporous crystalline diffusivity (a function of q_i^* and T)[22]. Assuming that the mass flux at the center of the particle ($r = 0$) is finite and the gas phase concentration outside the particle ($r = r_\mathrm{c}$) is constant, the following boundary conditions can be imposed:

$$\left.\frac{\partial q}{\partial r}\right|_{r=0} = 0 \tag{7}$$

$$q(r_\mathrm{c}) = q^*(p_i) \tag{8}$$

where $q^*(p_i)$ is a suitable isotherm model (the equilibrium loading of component i at a given pressure). For constant diffusivity systems, or for experiments where the change in the solid-phase concentration is small enough, D_c can be assumed to be a constant. When this condition is satisfied, an analytical solution for the transient mass uptake for a micropore limited system can be found[23]:

$$\frac{m_t}{m_\infty} = 1 - \frac{6}{\pi^2}\sum_{n=1}^{\infty}\frac{\exp(-n^2\pi^2\frac{D_\mathrm{c}}{r_\mathrm{c}^2}t)}{n^2} \tag{9}$$

The solution is an infinite series, with the only unknowns being D_c and r_c for a given experiment. These can be combined into a single parameter, $D_\mathrm{c}/r_\mathrm{c}^2$, also known as the pore diffusional time constant.

With the chemical potential gradient being the driving force for diffusion, the value of

D_c varies as a function of the solid-phase concentration. This typically follows Darken's relationship:

$$\frac{\partial \ln(p)}{\partial \ln(q^*)} = \frac{D_\mathrm{c}}{D_{\mathrm{c},0}} \tag{10}$$

where $D_{\mathrm{c},0}$, a function of T, is the limiting pore diffusion within the micropore. For the single-site Langmuir isotherm, Eqn. 10 can be written as:

$$\frac{D_\mathrm{c}}{D_{\mathrm{c},0}} = \frac{1}{1-\theta} \tag{11}$$

where θ is the fractional loading ($\theta_i = q_i^*/q_{\mathrm{b},i}^{\mathrm{sat}}$). Note that for a linear isotherm the derivative $\partial \ln(p)/\partial \ln(q^*) = 1$, therefore $D_\mathrm{c} = D_{\mathrm{c},0}$.

Surface Barrier Controlled: The second mechanism considers that the main mass transfer resistance is at the pore mouth. This is due to a pore mouth that is very small with respect to the micropore and adsorbate. Barrier resistance can arise from either pore blocking, where the surface of a material has few entry points for an adsorbate, or pore narrowing, where the pore mouth is significantly smaller than the micropore interior[24,25]. In this case, the micropore mass balance takes the form of a linear driving force model:

$$\frac{\partial \bar{q}}{\partial t} = k_\mathrm{b}(q^* - \bar{q}(t)) \tag{12}$$

where k_b is the barrier constant (a function of q_i^* and T)[22]. Solving the differential equation, for the case where q_i^* remains constant, the following analytical equation for the mass uptake when surface barrier resistance is dominant can be obtained:

$$\frac{m_t}{m_\infty} = 1 - \exp(-k_\mathrm{b} t) \tag{13}$$

The only unknown in the equation above is k_b, which can be determined with an experimental uptake curve. This model will be referred to as the surface barrier model.

Like the micropore model, the barrier constant, k_b, is known to be a function of the solid-phase loading. Accordingly, Darken's equation for the barrier constant can be written as:

$$\frac{\partial \ln(p)}{\partial \ln(q^*)} = \frac{k_\mathrm{b}}{k_{\mathrm{b},0}} \tag{14}$$

where $k_{\mathrm{b},0}$ (a function of T) is the limiting surface barrier resistance at the pore mouth. In the case of a single-site Langmuir isotherm, Darken's equation for the barrier constant is:

$$\frac{k_\mathrm{b}}{k_{\mathrm{b},0}} = \frac{1}{1-\theta} \tag{15}$$

which takes the same functional form as Eqn. 10[18].

Dual-resistance Model: The final model assumes that both the surface barrier and micropore contribute to the micropore resistance. This model describes a situation where the pore mouth is occluded and the micropore contributes to the diffusional resistance. The mass balance is the same as the micropore model (Eqn. 6) but the boundary condition at the surface changes to[18]:

$$\frac{3}{r_\mathrm{c}} D_\mathrm{c} \frac{\partial q(r_\mathrm{c})}{\partial r} = k_\mathrm{b}(q^* - \bar{q}(t)) \tag{16}$$

Solving the partial differential equation yields an analytical solution for the mass uptake when both the surface barrier and micropore resistances contribute to the mass transfer resistance:

$$\frac{m_t}{m_\infty} = 1 - \sum_{n=1}^{\infty} \frac{6L^2 \mathrm{exp}(-\beta_n^2 \frac{D_\mathrm{c}}{r_\mathrm{c}^2} t)}{\beta_n^2(\beta_n^2 + L(L-1))} \tag{17}$$

where β_n are the nonzero solutions to:

$$\beta_n \mathrm{cot} \beta_n + L - 1 = 0 \tag{18}$$

and

$$L = \frac{k_\mathrm{b} r_\mathrm{c}^2}{3D_\mathrm{c}} \tag{19}$$

There are two unknowns: k_b and $D_\mathrm{c}/r_\mathrm{c}^2$, that are fitted to experimental data. This model will be referred to as the dual-resistance model[21]. In the limiting case of a very large pore diffusion constant or barrier constant, the dual-resistance model reduces to either a surface barrier model or micropore model[18].

The analytical expressions presented above are only applicable either when the adsorption isotherm is linear or when the change in the solid phase loading is along a linear chord of the isotherm. However, when these limiting situations are no longer valid, exact analytical solutions cannot be derived. For such situations, the crystal radius is discretized into 1000 grid points and the general form of the transport equation, i.e., Eqn. 6, is solved numerically. The boundary condition at $r = 0$ is given by Eqn. 7. The boundary condition at $r = r_\mathrm{c}$ is given either by Eqn. 16 or 12, depending on whether a surface barrier is present, or not. The resulting ordinary differential equations were solved using *ode15s* in MATLAB. This numerical scheme was validated with the analytical models provided above and data from the literature that are shown in the Supporting Information (Fig. S3)

The experimental diffusion coefficients were determined using all three analytical models, as appropriate. For these experiments, the diffusivity was determined by minimizing the sum of squared error between the experimental and model uptake curves:

$$J_2 = \sum_{j=1}^{n} \left[\left(\frac{m_t}{m_\infty} \right)_{\mathrm{exp},j} - \left(\frac{m_t}{m_\infty} \right)_{\mathrm{model},j} \right]^2 \tag{20}$$

Kinetic Selectivity

The equilibrium selectivity, α_E, of a competitive mixture, A and B, is

$$\alpha_{\mathrm{E(A,B)}} = \frac{q_\mathrm{A}^*}{q_\mathrm{B}^*} \frac{y_\mathrm{B}}{y_\mathrm{A}} \tag{21}$$

where y is the gas phase mole fraction that is in equilibrium with the solid at a given temperature and total pressure[26]. To account for the differences in diffusivity between two gases, the kinetic selectivity, α_K, is defined as[12]:

$$\alpha_{\mathrm{K(A,B)}} = \frac{(m_t/m_\infty)_\mathrm{A}}{(m_t/m_\infty)_\mathrm{B}} \frac{q^*_\mathrm{A}}{q^*_\mathrm{B}} \frac{y_\mathrm{B}}{y_\mathrm{A}} \tag{22}$$

The kinetic selectivity approaches the equilibrium selectivity as time goes to infinity[12,21]. The kinetic selectivity in the Henry's law region can be approximated as:

$$\alpha_{\mathrm{K(A,B)}} = \frac{K_\mathrm{A}}{K_\mathrm{B}} \sqrt{\frac{(D_\mathrm{c,0})_\mathrm{A}}{(D_\mathrm{c,0})_\mathrm{B}}} \tag{23}$$

for the pore time diffusional time constant and

$$\alpha_{\mathrm{K(A,B)}} = \frac{K_\mathrm{A}}{K_\mathrm{B}} \frac{(k_\mathrm{b,0})_\mathrm{A}}{(k_\mathrm{b,0})_\mathrm{B}} \tag{24}$$

for the barrier constant where K_i is the Henry constant of component i, $D_\mathrm{c,0}$ is the limiting pore diffusion time constant and $k_\mathrm{b,0}$ is the limiting barrier coefficient[22]. Limiting constants are for a given temperature as the loading approaches zero. However, Eqns. 23 and 24 can only be used if there is only a single mass transfer resistance in the system.

Results and Discussion

Single Component Equilibrium

The equilibrium data for N_2 and CH_4 on both Ba-RPZ and zeolite 4A were measured, and the results are reported in Fig. 1. The N_2 and CH_4 isotherms for zeolite 4A are essentially linear at all temperatures and pressures, which allows them to be reasonably approximated with a linear isotherm and eliminates the need to use the Darken correction in the calculation of diffusivity. Both the N_2 and CH_4 isotherms for Ba-RPZ, however, are distinctly non-linear but could reasonably be described using a single-site Langmuir equation. The isotherm parameters for both adsorbents are listed in Table 1. The nonlinearity of the N_2

and CH_4 isotherms on Ba-RPZ required the use of the Darken correction in the calculation of the diffusivity of the two species. Because the Darken correction requires that the saturation capacity for the adsorbents be known, the saturation capacity for N_2 and CH_4 on Ba-RPZ was measured using the HPVA. The saturation capacity for Ba-RPZ was found to be 0.8 mol/kg and the associated high-pressure isotherms are provided in the Supporting Information (Fig. S4).

Figure 1 also shows the calculated ΔH_{iso} values for the two gases on both adsorbents. These values were calculated from 30 to 70°C and, from vacuum up to 1.2 bar, for both N_2 and CH_4 using numerical derivatives of Eqn. 4 at given values of q_i^*. The isosteric heat of N_2 ($\approx$ 25 kJ/mol), and CH_4 ($\approx$ 20 kJ/mol), are fairly constant over the calculated loading ranges. Since there is not a significant change in isosteric heat, both CH_4 and N_2 see the Ba-RPZ surface as essentially energetically homogeneous[27,28]. For zeolite 4A, the isosteric heats of both N_2 ($\approx$ 18 kJ/mol) and CH_4 ($\approx$ 18 kJ/mol) are essentially constant over the calculated loading ranges. It is interesting to note that the isosteric heats are the same for both gases on zeolite 4A.

Diffusion of N_2 and CH_4 in Zeolite 4A

Uptake curves for N_2 and CH_4 on zeolite 4A are shown in Fig. 2. The corresponding pressure curves, measured by the volumetric system, are given in the Supporting Information (Fig. S5). Uptake curves for CH_4 were measured at 30, 40 and 50°C at $\approx$ 300 mbar pressure steps between limiting vacuum and 1.2 bar. Uptake curves for N_2 were measured at -20, -10 and 0°C for the same pressure range. The uptake curves are plotted versus square root time to better visualize the shape of the initial uptake[21]. This plot allows for a qualitative determination of the mass transfer resistances: either the initial uptake will be linear (when plotted versus square root time) for a micropore controlled system or sigmoidal for a system that experiences significant barrier resistance (either surface barrier or dual-resistance modelled systems)[18].

Uptake on zeolite 4A data was studied as a reference to verify that the selected experimental conditions and equipment were able to reproduce uptake rates reported in the literature. Figure 2 shows the uptake of CH_4 as a function of square root time and demonstrates that, as anticipated, the initial CH_4 uptake is linear. This result confirms that the mass transfer resistance resides in the micropores of the adsorbent. This result is consistent with observations found in other studies[18,29,30]. Figure 2 also shows the measured N_2 uptake on zeolite 4A, which again reveals a micropore controlled system. The measured uptake curves for N_2 equilibrate significantly faster (by $\approx$ 300 s) compared to CH_4 on zeolite 4A. It should be noted that, in Fig. 2, for a particular gas at a given temperature, all of the individual uptake curves are virtually indistinguishable from each other. This result is characteristic of adsorption systems having linear isotherms.

The pore diffusion time constants fitted from the uptake curves are plotted in Fig. 3 as a function of the adsorbate loading. The data was fit to Darken's equation, and the results of the fit are shown alongside the experimental data. The results establish that, for zeolite 4A, the diffusion time constant does not change significantly as the adsorbate loading is increased. The limiting transport parameters are shown in Table 2 and were determined by calculating the average of $D_{\mathrm{c},i}$ over the loading range studied. The 95% confidence intervals are also shown alongside the value. A comparison of the measured limiting diffusivities and values from the literature is shown in Table 3. As seen in Table 3, our limiting diffusivities are comparable to what has been previously reported. The pore diffusional time constants for N_2 and CH_4 on zeolite 4A were nicely fit with the predictions from Darken's equation. Since a linear isotherm was used, Darken's equation reduces to $D_{\mathrm{c}} = D_{\mathrm{c,0}}$. This behaviour is consistent with other studies[6,31].

The temperature dependence of the diffusion parameters on zeolite 4A was determined at 30, 40 and 50°C for CH_4 and -20, -10 and 0°C for N_2 using an Arrhenius relationship in Fig. 4. The slope was determined from a plot of $\ln(D_{\mathrm{c,0}}/r_{\mathrm{c}}^2)$ versus $1/T$. This yields a straight line where the slope is $-E_{\mathrm{a,d}}/R$, where $E_{\mathrm{a,d}}$ is the micropore activation energy and R

is the universal gas constant. The exponent of the intercept yields the Arrhenius prefactor. This model can be used in tandem with a concentration dependence model to predict gas uptake. Activation energies for N_2 and CH_4 on 4A are shown in Table 2. The activation energies are used with the following equation to estimate the limiting transport parameters as a function of temperature:

$$D_{\mathrm{c},0} = D'_{\mathrm{c},0}\exp\left(\frac{-E_{a,\mathrm{d}}}{RT}\right) \tag{25}$$

The calculated activation energy of CH_4 (22.93 kJ/mol) and N_2 (20.86 kJ/mol) on zeolite 4A was determined to be within the range of previously reported values. A few papers provide this information, with $E_{a,\mathrm{d}}$ ranging from 18.66 to 26.78 kJ/mol for CH_4 and 19.00 to 23.43 kJ/mol for N_2 in the range of temperatures measured in this study[6,29–31]. This data is also shown in Table 3 to compare our measurements to the literature. The agreement between the zeolite 4A data collected during this study and previous studies provides confidence that the instrumentation and techniques being used are capable of providing quantitative diffusivity data.

Diffusion of N_2 and CH_4 in Ba-RPZ

The measurement of N_2 and CH_4 diffusivity in the titanosilicate Ba-RPZ was carried out in a manner similar to the one described for zeolite 4A. Certain adaptations were required to accommodate the differences in adsorptive characteristics between zeolite 4A and Ba-RPZ. Similar experimental temperatures were used for the two adsorbates, but the non-linear isotherms for N_2 and CH_4 on Ba-RPZ required a specific dosing protocol. The dose quantity for either N_2 or CH_4 was selected to ensure that the change in adsorbate loading on the solid was maintained within a linear portion of the related isotherm. Selecting small dose quantities helps to ensure that the diffusion rate for the adsorbate will be effectively constant throughout the course of the uptake experiment. The adsorbate doses selected to maintain a constant diffusivity are, herein, termed “small” doses. The curvature of the N_2 and CH_4 isotherms for Ba-RPZ also provides an opportunity to measure how the diffusivity changes across a non-linear portion of the isotherm. The dose quantities of adsorbate required to move across a broader section of the isotherm were correspondingly larger and are termed “large” doses. Uptake curves for CH_4 were measured at 30, 40 and 50°C at $\approx$ 15 to 300 mbar pressure steps between limiting vacuum and 1.2 bar. Uptake curves for N_2 were measured at -17, -10 and 0°C for the same pressure range.

Figure 5 provides the measured uptake profiles for N_2 and CH_4 on Ba-RPZ. The corresponding pressure curves are given in the Supporting Information (Fig. S6). The diffusional resistance that N_2 experienced on Ba-RPZ was found to be comparable to that of zeolite 4A. As a result, it was necessary to measure the N_2 uptake curves at sub-ambient temperatures. It can be seen that even at -17°C the initial uptake for N_2 is linear, which indicates that the diffusional resistance is primarily microporous in nature. This result suggests that N_2 is able to access and diffuse through the Ba-RPZ structure without any special restriction to its movement.

In contrast to the N_2 uptake curves, the initial uptake curves for CH_4 adsorption display a sigmoidal shape, which indicates the presence of a barrier resistance. The presence of a barrier resistance indicates that the adsorbent features a constriction which is on the order of the molecular diameter of the methane and serves to significantly impede the rate of diffusivity. The barrier resistance is most pronounced at the lowest temperature studied (30°C) and became less pronounced as the temperature increases.

The surface barrier model (Eqn. 12) alone was not able to accurately match the entire experimental uptake curves. While the initial sigmoidal shape could be accurately described using the surface barrier model, the model predicts CH_4 equilibrium sooner than what is experimentally observed. This result suggests that there is also a non-negligible transport resistance within the micropores. A hybrid model was constructed that incorporated both barrier and microporous elements, and it was found that this dual-resistance model was able to acceptably describe the experimental uptake profiles. A comparison of the three mathematical models (micropore, barrier, and barrier plus micropore) with a typical experimental CH_4 uptake curve on Ba-RPZ is shown in Fig. 6. The dual-resistance model was used to describe each uptake curve of CH_4 (k_b and $D_\mathrm{c}/r_\mathrm{c}^2$ values were fitted) while the micropore model was used to describe each uptake curve of N_2 ($D_\mathrm{c}/r_\mathrm{c}^2$ values were fitted).

Figure 7 shows the concentration dependence (in fractional loading $\theta_i = q_i^*/q_{\mathrm{b},i}^{\mathrm{sat}}$) of CH_4 and N_2 diffusion on Ba-RPZ. It is worth noting that this figure contains all of the diffusivity data collected, including repeated experiments. The micropore diffusion time constants for both N_2 and CH_4 on Ba-RPZ were in good agreement with the predictions from Darken's equation. The barrier constant was modelled using an empirical equation:

$$\frac{k_\mathrm{b}}{k_{\mathrm{b},0}} = \exp(\beta_\mathrm{b}\theta) \tag{26}$$

where $\beta_\mathrm{b} = 5.223$ was fitted to the experimental data. Figure 7(c) shows both Darken's prediction and the empirical fit for the barrier constant. While the Darken equation could be forced to follow the barrier constant at low fractional loadings, no parameters were found that would allow the Darken equation to describe the barrier constant trend across the full range of fractional loadings. The trend in the barrier constant as a function of CH_4 fractional loading indicates that the rate of diffusion of methane in the barrier increases faster than the rate of change in the chemical potential at the sieve surface. As the fractional loading increases, the rate of diffusion across the barrier increases and, at a certain point, the barrier diffusion rate is so high that a sigmoidal shape is no longer evident in the uptake curves. The absence of the sigmoidal shape signals that the contribution of the barrier resistance has become negligible and, beyond this point, the diffusion becomes dominated by micropore resistance. As a result, the barrier constant calculations are only included up to $\theta_{CH_4} = 0.5$. A sensitivity analysis is given in the Supporting Information (Fig. S7) to show that at $\theta_{CH_4} > 0.5$, the calculation of the barrier constant fitting becomes unreliable because any suitably large k_b can be used to fit the uptake curve.

The calculated limiting transport parameters are shown in Table 2 and were determined at a given temperature by minimizing the squared error between all collected data with an assumed concentration dependence model, such as Darken's equation. The following objective functions were used for the micropore and surface-barrier constants, respectively:

$$J_3 = \sum_{j=1}^{n} \left[\left(\log_{10}\left(\frac{D_\mathrm{c}}{r_\mathrm{c}^2} \right) \right)_{\mathrm{exp},j} - \left(\log_{10}\left(\frac{D_\mathrm{c}}{r_\mathrm{c}^2} \right) \right)_{\mathrm{model},j} \right]^2 \tag{27}$$

$$J_4 = \sum_{j=1}^{n} \left[\left(\log_{10}(k_\mathrm{b}) \right)_{\mathrm{exp},j} - \left(\log_{10}(k_\mathrm{b}) \right)_{\mathrm{model},j} \right]^2 \tag{28}$$

A logarithm was used to yield a better estimate of the limiting diffusivities at low values of θ. The limiting diffusivities for CH_4 were used to determine the ratio $k_{\mathrm{b},0}/(D_{\mathrm{c},0}/r_\mathrm{c}^2)$ as a function of temperature. This relation is expected to be constant if the surface barrier resistance is due to pore blocking (limited access to the crystal but facile diffusion within it), while it will not be constant if the surface barrier resistance is due to narrowing at the pore mouth (pore entrances approach the molecular diameter of the adsorbate)[24]. The ratio of the barrier resistance to the micropore diffusivity (shown in the Supporting Information in Fig. S8) increases with temperature indicating that surface barrier resistance in Ba-RPZ is consistent with a narrowing of the pore mouth relative to the micropore interior. It should be noted that neither the data nor the model can determine whether the barrier resistance exists at the surface of the crystals or within the structure of the molecular sieve, i.e., an internal barrier[32].

The temperature dependence of the CH_4 and N_2 diffusivities on Ba-RPZ was calculated in the same way as was described for zeolite 4A and are likewise presented in Fig. 4. For Ba-RPZ, the Arrhenius relationship for both the micropore and barrier resistances were plotted to determine the activation energies from either $\ln(k_{\mathrm{b},0})$ or $\ln(D_{\mathrm{c},0}/r_\mathrm{c}^2)$ versus $1/T$. The calculated activation energies are shown in Table 2. The activation energies are used with Eqn. 25 and the following analogue for the barrier resistance to estimate the limiting diffusivities as a function of temperature:

$$k_{\mathrm{b},0} = k'_{\mathrm{b},0}\exp\left(\frac{-E_{a,\mathrm{b}}}{RT}\right) \tag{29}$$

The micropore activation energies for CH_4 on Ba-RPZ was calculated to be $E_{a,\mathrm{d}} = 30.46$ kJ/mol and the barrier resistance activation energy was calculated to be $E_{a,\mathrm{b}} = 60.19$ kJ/mol. For N_2, a micropore diffusion activation energy was calculated to be $E_{a,\mathrm{d}} = 25.77$ kJ/mol. The activation energies for both N_2 and CH_4 on Ba-RPZ are significantly larger than those found for zeolite 4A, which will make the diffusion of N_2 and CH_4 in Ba-RPZ a strong function of temperature. The difference in activation energy between the barrier and micropore $(E_{a,\mathrm{b}} - E_{a,\mathrm{d}})$ is ≈ 30 kJ/mol and is consistent with the observation of an internal barrier for n-butane in silicalite[32].

Model Validation

The sigmoidal shape presented by the methane uptake experiments on Ba-RPZ signifies the presence of a restriction in the molecular sieve that has a significant influence on the diffusion of CH_4. The uptake data were described using a dual-resistance model, which assumed that two independent resistances (barrier and micropore) are present in the molecular sieve. The proposed adsorption mechanism for Ba-RPZ, however, describes a crystalline adsorbent having a highly uniform channel system incorporating a series of halogen obstructions[17]. While the mathematical construct of the dual-resistance model used in this work may not perfectly reflect the adsorption mechanism proposed for Ba-RPZ, such incongruity does not infer that the model cannot accurately predict the adsorptive behaviour of the sieve. Being able to accurately describe the diffusion behaviour of a molecular sieve mathematically is a critical step in being able to predict the performance of that adsorbent in selected adsorptive separations.

A series of large dose experiments were performed at 30, 40 and 50°C to understand whether the dual-resistance model could accurately predict complex diffusion behaviour. As was previously mentioned, diffusivity is a function of solid loading, and so a large dose creates a non-linear change in loading to deliberately generate a constantly changing diffusivity. The associated uptake data can thus be used to validate whether the diffusion model (which was constructed from the small dose, constant-diffusivity experiments) can successfully predict complex diffusion behavior. The full numerical solution to Eqn. 6 is required along with an appropriate concentration dependence model to describe the large-dose experiment. The resulting concentration-dependent dual-resistance model is expected to be able to predict the changing diffusivity behavior evident in the large dose experiments.

The results from the large dose experiments are shown in Fig. 8. The central curve in black in Fig. 8(a) represents an experiment carried out at 30°C where a single dose of CH_4 was used to move the equilibration pressure from limiting vacuum (5 μbar) to 211.1 mbar. The small dose (constant diffusivity) experiments that bound this large dose experiment are also presented in Fig. 8(a). The lower pressure small dose from 0 to 19.2 mbar (which resides in the limiting diffusivity region) is shown in red and the higher pressure small dose, from 176.6 to 218.3 mbar, is shown in blue. The large dose curve initially follows the red, limiting diffusion curve until ≈ 30 $s^{0.5}$ where the curve inflects, signifying that diffusion is becoming more rapid. As time proceeds, the profile of the large dose curve mirrors that of the blue, higher pressure small dose. The concentration-dependent dual-resistance model was used to describe all three curves, and the results are shown as solid lines in the corresponding colour. The concentration-dependent dual-resistance model generally fits the large dose data in Fig. 8(a) well, although it does predict a more rapid uptake and trend to equilibrium compared to the experimental data. The independent, small dose curves were also described using the concentration-dependent dual-resistance model, and the results show that the model can accurately describe the uptake curve for the constant diffusivity experiments as well. The same experiments and calculations were carried out for CH_4 on Ba-RPZ at 40 and 50°C and the results are provided Fig. 8(b) and 8(c), respectively. As was observed for the experiment at 30°C, the large dose curve follows the limiting diffusion curve at short times and the higher pressure constant diffusivity curve closer to equilibrium. As was seen with the 30°C data, the concentration-dependent dual-resistance model provided a good description of the experimental large dose experiments, although some discrepancy is noted. Likewise, the concentration-dependent dual-resistance model was able to accurately describe the independent constant diffusivity experiments that bounded each large-dose experiment at sequentially higher temperatures. The concentration-dependent dual-resistance model can thus be used to accurately predict complex diffusion behaviour across both temperature and pressure for Ba-RPZ.

Kinetic Selectivity

Having established the diffusion mechanisms and the equilibrium, the kinetic selectivity for a N_2/CH_4 gas mixture can be calculated. The kinetic selectivities for zeolite 4A, Sr-ETS-4 and Ba-RPZ were determined at 10°C for an 80/20 mol% mixture of CH_4/N_2 from zero loading to 1 bar. This temperature was selected because comparable data for Sr-ETS-4 was available at this temperature and because 10°C represents only a mild extrapolation for measured data for N_2 and CH_4. The full solution for each individual adsorbate uptake was solved, as per Eqn. 22, to determine the kinetic selectivity as a function of time for all adsorbents. The full numerical solution of the micropore and dual-resistance models assumed that the diffusivities followed a concentration-dependence model (found and validated in the previous sections) and that there is no equilibrium competition between CH_4 and N_2. For CH_4 on Ba-RPZ, both the barrier and micropore resistances were accounted for when determining the kinetic selectivity. Figure 9(a) demonstrates that, at low contact times, the kinetic selectivity on Ba-RPZ is greater than 1000. This selectivity is generated almost exclusively by the barrier resistance that Ba-RPZ imposes on CH_4 because N_2, by contrast, is effectively equilibrium controlled at 10°C. As the contact time proceeds, the N_2/CH_4 selectivity decreases as the kinetic selectivity collapses toward the equilibrium selectivity. It should be noted that even after a contact time of 1000s Ba-RPZ has not reached equilibrium.

The calculated kinetic selectivities for zeolite 4A and Sr-ETS-4 is also shown in Fig. 9(a). The rapid decrease in selectivity noted at short times for zeolite 4A is not due to a barrier resistance because the diffusion behaviour in this molecular sieve is micropore-controlled for both N_2 and CH_4. The results reflect that zeolite 4A loses its kinetic selectivity as it rapidly approaches equilibrium at around 300 s. The Sr-ETS-4 equilibrium and kinetic data used in the calculation of the kinetic selectivity were calculated from Marathe *et al.*[13]. The diffusion of N_2 and CH_4 in Sr-ETS-4 has been demonstrated to be solely micropore controlled. The kinetic selectivity for Sr-ETS-4 does not display the barrier resistance influence seen with Ba-RPZ, nor does it reach equilibrium as quickly as zeolite 4A. These results imply that the effective pore size of Sr-ETS-4 likely falls somewhere between 4A and Ba-RPZ. While the calculated micropore diffusion time constants for the two titanosilicates are comparable[12] the presence of the barrier resistance to CH_4 in Ba-RPZ distinguishes this adsorbent and gives rise to its exceptional kinetic selectivity.

Figure 9(b) shows the limiting kinetic selectivity calculated for Ba-RPZ and Sr-ETS-4 using an 80/20 mol% mixture of CH_4/N_2 at 1 bar at temperatures between 0 and 70°C. The limiting kinetic selectivity is defined here as the kinetic selectivity value at $t \to 0$ s. The trend displayed for Ba-RPZ shows that the limiting kinetic selectivity progressively decreases as temperature increases. This trend is governed by methane diffusion in the sieve because the activation energy for diffusion in Ba-RPZ is much greater for CH_4 than it is for N_2. Sr-ETS-4, by contrast, demonstrates a limiting kinetic selectivity that increases slightly with temperature.

The diffusivity behaviour that Ba-RPZ displays toward N_2 and CH_4 is unique. The presence of a barrier resistance for methane and the relatively free diffusion of N_2 suggests that the mode of transport for these two gases within the pores and channels of Ba-RPZ is unlike similar small-pored molecular sieves. The complex diffusivity behaviour can be accurately described using existing diffusion models, and the remarkable kinetic selectivity displayed by the molecular sieve seems to make it an ideal candidate for addressing nitrogen contamination in natural gas wells.

Conclusions

A detailed study of the adsorption of N_2 and CH_4 on Ba-RPZ was completed. The thermodynamics of adsorption were determined, and the diffusivity rates for the two adsorbates were measured. It was found that, under the conditions explored, N_2 diffusion is microporous in nature and encounters little resistance to entering and diffusing through the Ba-RPZ framework. This was not the case for methane, where it was found that the Ba-RPZ framework exerts a strong barrier resistance toward CH_4 which significantly impedes the diffusion into or through the adsorbent crystals. The complex diffusion behaviour of CH_4 could be described using a concentration-dependent dual-resistance diffusion model which incorporated both barrier and microporous diffusion elements. The model was challenged, experimentally, using large dose methane uptake experiments, and it was found that the model was able to successfully describe the complex transition from barrier-limited diffusion to micropore-limited diffusion across a range of temperatures. The exact nature of the origin of the barrier resistance, i.e., external or internal barrier, could not be firmly established. Nevertheless, it was found Ba-RPZ can offer kinetic selectivities that can be orders of magnitude greater than current benchmark material for CH_4 upgrading, namely, Sr-ETS-4. The barrier resistance contributes significantly to this selectivity improvement. The results here suggest that Ba-RPZ could be a potential candidate for CH_4 upgrading. Recent literature for equilibrium separations that metrics such as selectivity are rather poor predictors of process performance[33–36]. Therefore, further studies will explore the potential of Ba-RPZ at a process scale.

Acknowledgments

This paper is dedicated to Prof. Giuseppe Storti, Politechnico Milano on the occasion of his 65th birthday. AR fondly remembers Prof. Storti's scientific rigour, his kindness, and the care he took in mentoring young researchers. The authors would like to thank Extraordinary Adsorbents Inc. (Edmonton, Alberta in Canada, www.extraordinaryadsorbents.com) for the crystalline Ba-RPZ sample and Prof. Steven M. Kuznicki, University of Alberta and Extraordinary adsorbents for discussions. Funding from NSERC through the Discovery program is acknowledged. Discussions with Prof. Shamsuzzaman Farooq, National University of Singapore, Singapore, are acknowledged.

Declaration of Interests

All authors confirm that there is no conflict of interest to declare.

Supporting Information

Supporting information containing determination of the activation temperature, model validation with literature uptake curves, SEM images of Ba-RPZ and zeolite 4A, high-pressure Ba-RPZ isotherms, pressure measurements in the dosing cell, sensitivity of fitting barrier resistance constants are available as a pdf file. An excel file containing numerical values of the equilibrium and kinetic measurements is also provided. This information is available free of charge via the Internet at http://pubs.acs.org/

Nomenclature

Roman symbols

b	adsorption equilibrium constant [m^3 mol^{-1}]
D	diffusivity [m^2 s^{-1}]
E	activation energy [J mol^{-1}]
ΔH	heat of adsorption [J mol^{-1}]
J	objective function [-]
k	barrier constant [s^{-1}]
K	Henry constant [m^3 kg^{-1}]
L	dual-resistance model parameter [-]
m	adsorbent mass [kg]
n	index [-]
p	partial pressure [bar]
q	solid phase loading [mol kg^{-1}]
q^*	equilibrium solid phase loading [mol kg^{-1}]
r	radius [m]
R	universal gas constant [Pa m^3 mol^{-1} K^{-1}]
t	time [s]
T	temperature [K]
y	mole fraction [-]

Greek symbols

α	selectivity [-]
θ	fractional loading [-]

Abbreviations, subscripts and superscripts

A	species A
B	species B
b	barrier
c	crystalline
comp	component
E	equilibrium
exp	experimental
i	index of species
∞	at equilibrium
j	index
K	kinetic
iso	isosteric
n	index
p	particle
sat	ultimate saturation
t	time
0	limiting

Acronyms

ETS	Engelhard titanosilicate
HPVA	high pressure volumetry apparatus
LDF	linear driving force
PSA	pressure-swing adsorption
ROA	rate of adsorption
RPZ	reduced pore zorite

SEM	scanning electron microscopy
SSL	single-site Langmuir model

References

1. Rufford, T. E.; Smart, S.; Watson, G. C. Y.; Graham, B. F.; Boxall, J.; Diniz da Costa, J. C.; May, E. F. The removal of CO_2 and N_2 from natural gas: A review of conventional and emerging process technologies. *J. Petrol. Sci. Eng.* **2012**, *94*, 123–154.

2. Bhatt, T. S.; Sliepcevich, A.; Storti, G.; Rota, R. Experimental and modeling analysis of dual-reflux pressure swing adsorption process. *Ind. Eng. Chem. Res.* **2014**, *53*, 13448–13458.

3. Erden, L.; Ebner, A. D.; Ritter, J. A. Separation of Landfill Gas CH_4 from N_2 Using Pressure Vacuum Swing Adsorption Cycles with Heavy Reflux. *Energy Fuels* **2018**, *32*, 3488–3498.

4. Effendy, S.; Xu, C.; Farooq, S. Optimization of a pressure swing adsorption process for nitrogen rejection from natural gas. *Ind. Eng. Chem. Res.* **2017**, *56*, 5417–5431.

5. Cavenati, S.; Grande, C. A.; Rodrigues, A. E. Separation of methane and nitrogen by adsorption on carbon molecular sieve. *Sep. Sci. Tech.* **2005**, *40*, 2721–2743.

6. Ahn, H.; Yoo, H.; Shul, Y.; Hyun, S.; Lee, C. Diffusion mechanism of N_2 and CH_4 in pelletized zeolite 4A, 5A and CaX. *J. Chem. Eng. Jpn* **2002**, *35*, 334–345.

7. Seabra, R.; Ribeiro, A. M.; Gleichmann, K.; Ferreira, A. F. P.; Rodrigues, A. E. Adsorption equilibrium and kinetics of carbon dioxide, methane and nitrogen on binderless zeolite 4A adsorbents. *Microporous and Mesoporous Mater.* **2019**, *277*, 105–114.

8. Jayaraman, A.; Hernandez-Maldonado, A. J.; Yang, R. T.; Chinn, D.; Munson, C. L.; Mohr, D. H. Clinoptilolites for nitrogen/methane separation. *Chem. Eng. Sci.* **2004**, *59*, 2407–2417.

9. Kennedy, D.; Tezel, F. Cation exchange modification of clinoptilolite–screening analysis

for potential equilibrium and kinetic adsorption separations involving methane, nitrogen, and carbon dioxide. *Microporous and Mesoporous Mater.* **2018**, *262*, 235–250.

10. Kuznicki, S. M.; Bell, V. A.; Petrovic, I.; Desai, B. T. Small-pored crystalline titanium molecular sieve zeolites and their use in gas separation processes. 2000; US Patent 6,068,682.
11. Marathe, R. P.; Mantri, K.; Srinivasan, M. P.; Farooq, S. Effect of ion exchange and dehydration temperature on the adsorption and diffusion of gases in ETS-4. *Ind. Eng. Chem. Res.* **2004**, *43*, 5281–5290.
12. Majumdar, B.; Bhadra, S. J.; Marathe, R. P.; Farooq, S. Adsorption and diffusion of methane and nitrogen in barium exchanged ETS-4. *Ind. Eng. Chem. Res.* **2011**, *50*, 3021–3034.
13. Marathe, R. P.; Farooq, S.; Srinivasan, M. P. Modeling gas adsorption and transport in small-pore titanium silicates. *Langmuir* **2005**, *21*, 4532–4546.
14. Bhadra, S. J.; Farooq, S. Separation of methane–nitrogen mixture by pressure swing adsorption for natural gas upgrading. *Ind. Eng. Chem. Res.* **2011**, *50*, 14030–14045.
15. Ansón, A.; Kuznicki, S. M.; Kuznicki, T.; Dunn, B. C.; Eyring, E. M.; Hunter, D. B. Separation of argon and oxygen by adsorption on a titanosilicate molecular sieve. *Sep. Sci. Technol.* **2009**, *44*, 1604–1620.
16. Sawada, J. A.; Rode, E. J.; Kuznicki, S. M.; Lin, C. C. I. Silicate materials, method for their manufacture, and method for using such silicate materials for adsorptive fluid separations. 2013; US Patent 8,545,608.
17. Lin, C. C. H.; Sawada, J. A.; Wu, L.; Haastrup, T.; Kuznicki, S. M. Anion-controlled pore size of titanium silicate molecular sieves. *J. Am. Chem. Soc.* **2008**, *131*, 609–614.

18. Qinglin, H.; Sundaram, S. M.; Farooq, S. Revisiting transport of gases in the micropores of carbon molecular sieves. *Langmuir* **2003**, *19*, 393–405.

19. Wang, J.; Mangano, E.; Brandani, S.; Ruthven, D. M. A review of common practices in gravimetric and volumetric adsorption kinetic experiments. *Adsorption* **2020**, 1–24.

20. Ruthven, D. M.; Farooq, S.; Knaebel, K. S. Pressure Swing Adsorption. *New York: VCH Publishers* **1994**, *1*, 235.

21. Jin, X.; Malek, A.; Farooq, S. Production of argon from an oxygen-argon mixture by pressure swing adsorption. *Ind. Eng. Chem. Res.* **2006**, *45*, 5775–5787.

22. Kärger, J.; Ruthven, D. M.; Theodorou, D. N. *Diffusion in nanoporous materials*; John Wiley & Sons, 2012.

23. Crank, J. *Mathematics of Diffusion*; Oxford University Press, 1956.

24. Ruthven, D. M.; Kärger, J.; Brandani, S.; Mangano, E. Sorption Kinetics: Measurement of Surface Resistance. *Adsorption* **2020**, 1–13.

25. Sastre, G.; Kärger, J.; Ruthven, D. M. Surface barriers and symmetry of adsorption and desorption processes. *Adsorption* **2020**, 1–9.

26. Ruthven, D. M. *Principles of Adsorption and Adsorption Processes*; John Wiley & Sons, 1984.

27. Sircar, S.; Cao, D. V. Heat of adsorption. *Chem. Eng. Tech.* **2002**, *25*, 945–948.

28. Sircar, S. Comments on practical use of Langmuir gas adsorption isotherm model. *Adsorption* **2017**, *23*, 121–130.

29. Yucel, H.; Ruthven, D. M. Diffusion in 4A zeolite. Study of the effect of crystal size. *J. Chem. Soc. Faraday Trans.* **1980**, *76*, 60–70.

30. Haq, N.; Ruthven, D. M. Chromatographic study of sorption and diffusion in 4A zeolite. *J. Colloid and Interf. Sci.* **1986**, *112*, 154–163.

31. Cao, D. V.; Mohr, R. J.; Rao, M. B.; Sircar, S. Self-diffusivities of N_2, CH_4, and Kr on 4A zeolite pellets by isotope exchange technique. *J. Phys. Chem. B* **2000**, *104*, 10498–10501.

32. Vasenkov, S.; Kärger, J. Evidence for the existence of intracrystalline transport barriers in MFI-type zeolites: a model consistency check using MC simulations. *Microporous Mesoporous Mater.* **2002**, *55*, 139–145.

33. Rajagopalan, A. K.; Avila, A. M.; Rajendran, A. Do adsorbent screening metrics predict process performance? A process optimisation based study for post-combustion capture of CO_2. *Int. J. Greenh. Gas. Cont.* **2016**, *46*, 76–85.

34. Burns, T. D.; Pai, K. N.; Subraveti, S. G.; Collins, S. P.; Krykunov, M.; Rajendran, A.; Woo, T. K. Prediction of MOF performance in vacuum swing adsorption systems for postcombustion CO_2 capture based on integrated molecular simulations, process optimizations, and machine learning models. *Env. Sci. Technol.* **2020**, *54*, 4536–4544.

35. Khurana, M.; Farooq, S. Adsorbent screening for postcombustion CO_2 capture: a method relating equilibrium isotherm characteristics to an optimum vacuum swing adsorption process performance. *Ind. Engg. Chem. Res.* **2016**, *55*, 2447–2460.

36. Park, J.; Rubiera Landa, H. O.; Kawajiri, Y.; Realff, M. J.; Lively, R. P.; Sholl, D. S. How Well Do Approximate Models of Adsorption-Based CO_2 Capture Processes Predict Results of Detailed Process Models? *Ind. Engg. Chem. Res.* **2019**, *59*, 7097–7108.

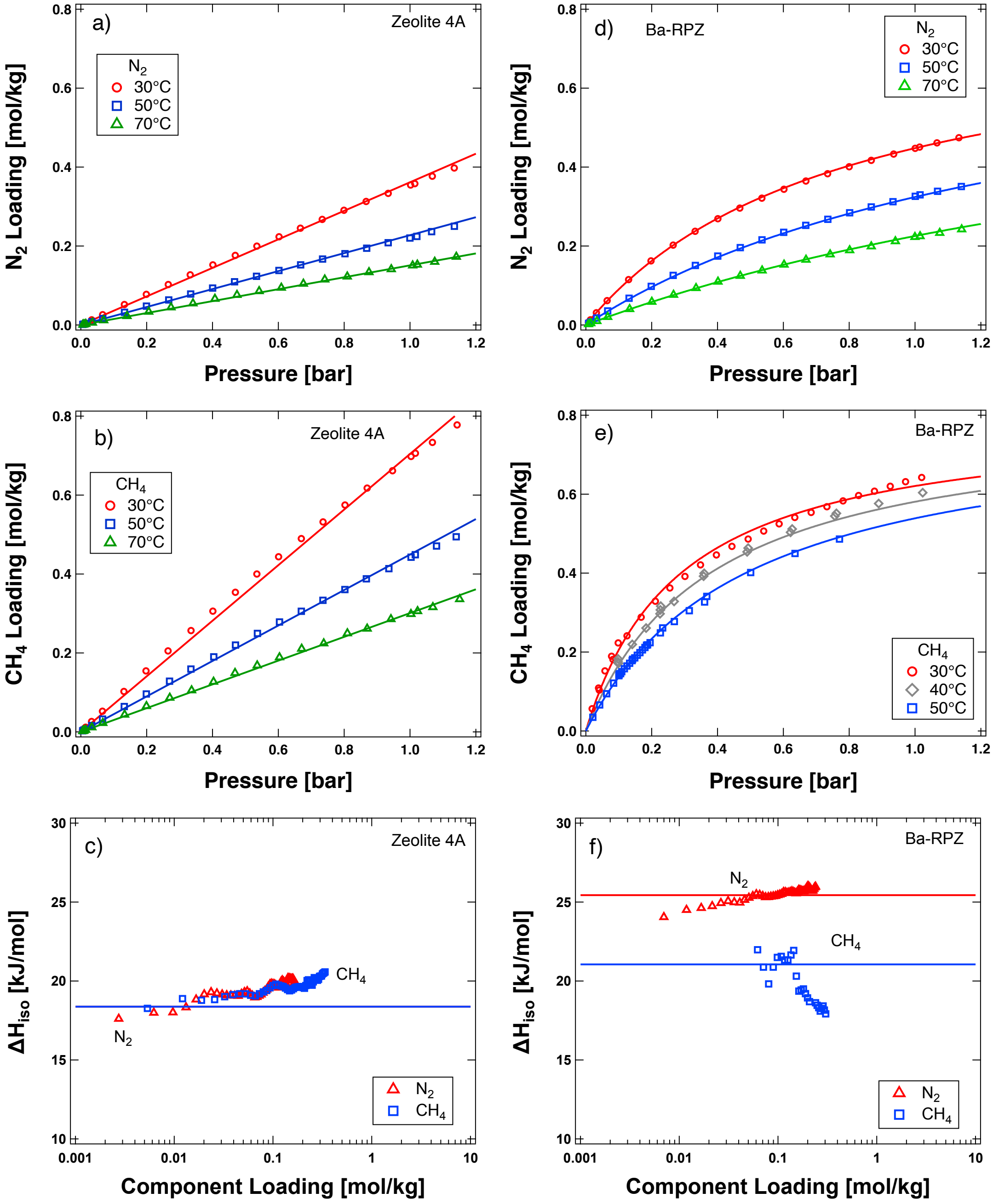

Figure 1: Single component adsorption equilibrium on zeolite 4A crystals for (**a**) N_2 and (**b**) CH_4 with linear isotherm fits and Ba-RPZ for (**d**) N_2 and (**e**) CH_4 with single-site Langmuir isotherm fits. Panels (**c**) and (**f**) show the isosteric heats of CH_4 and N_2 on zeolite 4A and Ba-RPZ, respectively. The isosteric heats are shown with the predictions from the isotherm models. Note that for zeolite 4A, the model predicts nearly identical heats of adsorption.

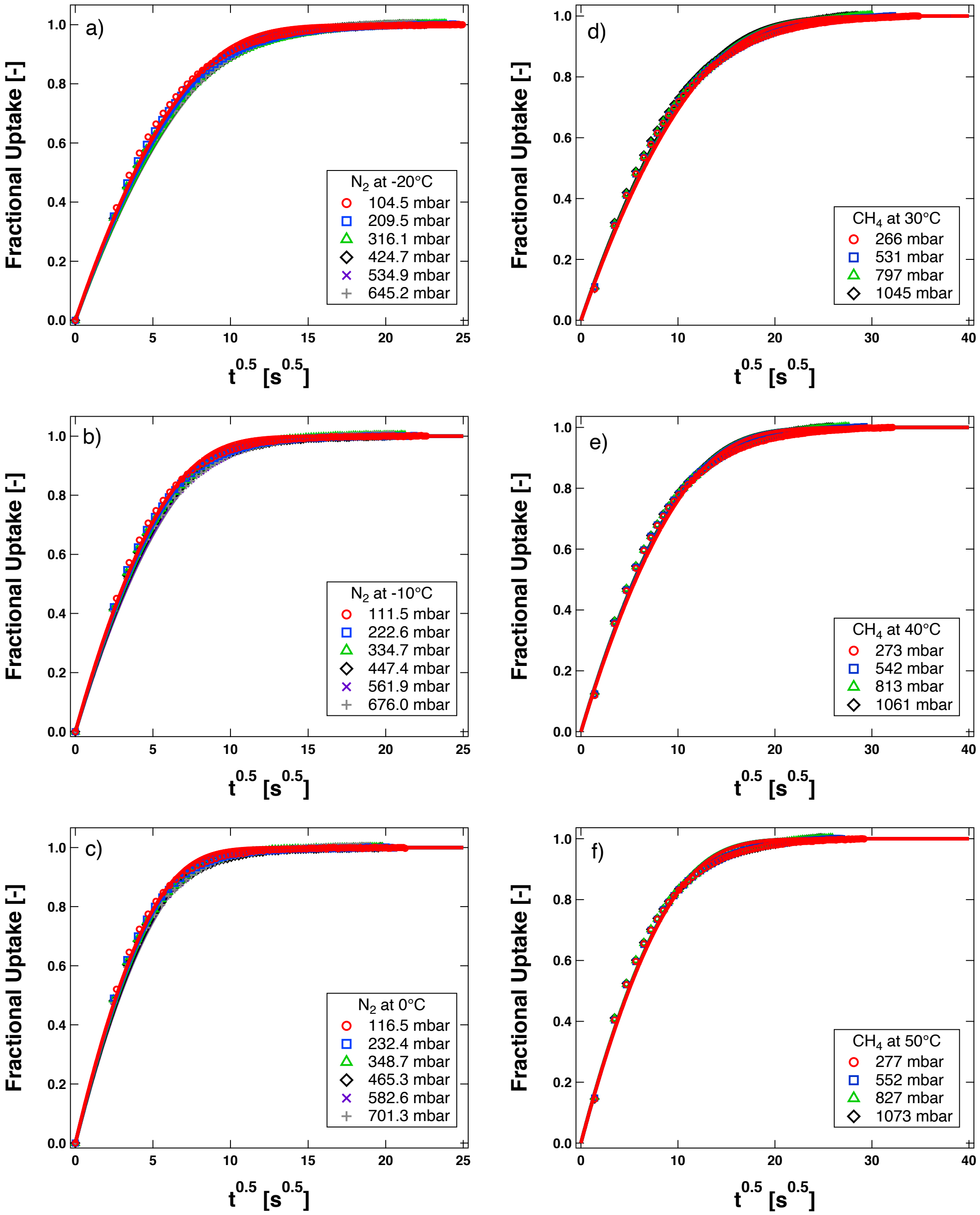

Figure 2: Constant diffusivity uptake curves for N_2 at (**a**) -20, (**b**) -10 and (**c**) 0°C and CH_4 at (**d**) 30, (**e**) 40 and (**f**) 50°C on zeolite 4A crystals. The lines show the micropore model fits. Note that every fifth experimental point is plotted to better show the model fit.

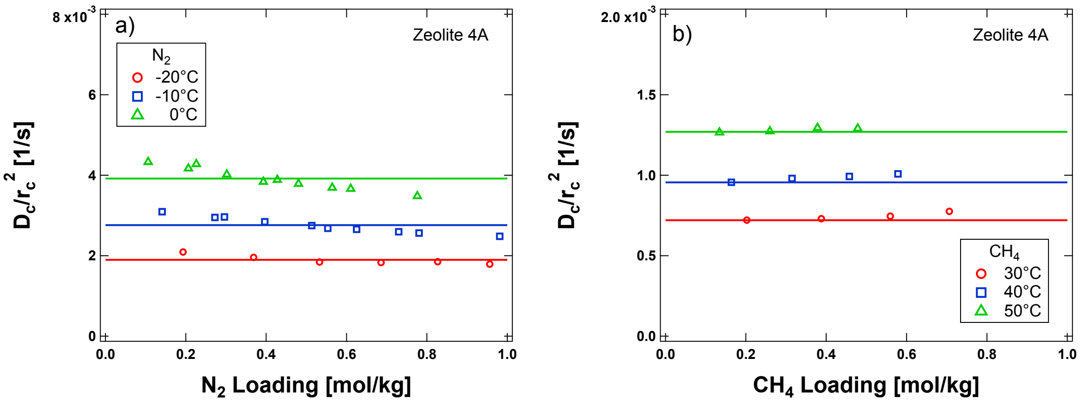

Figure 3: Pore diffusion time constants as a function of solid phase concentration for (**a**) N_2 and (**b**) CH_4 on zeolite 4A. The data is overlaid with predictions by Darken's equation (lines).

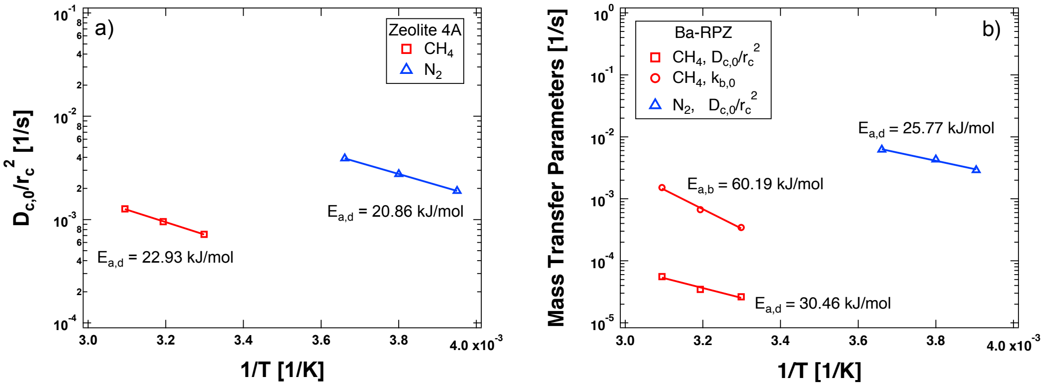

Figure 4: Activation energies of N_2 and CH_4 on (**a**) zeolite 4A and (**b**) Ba-RPZ.

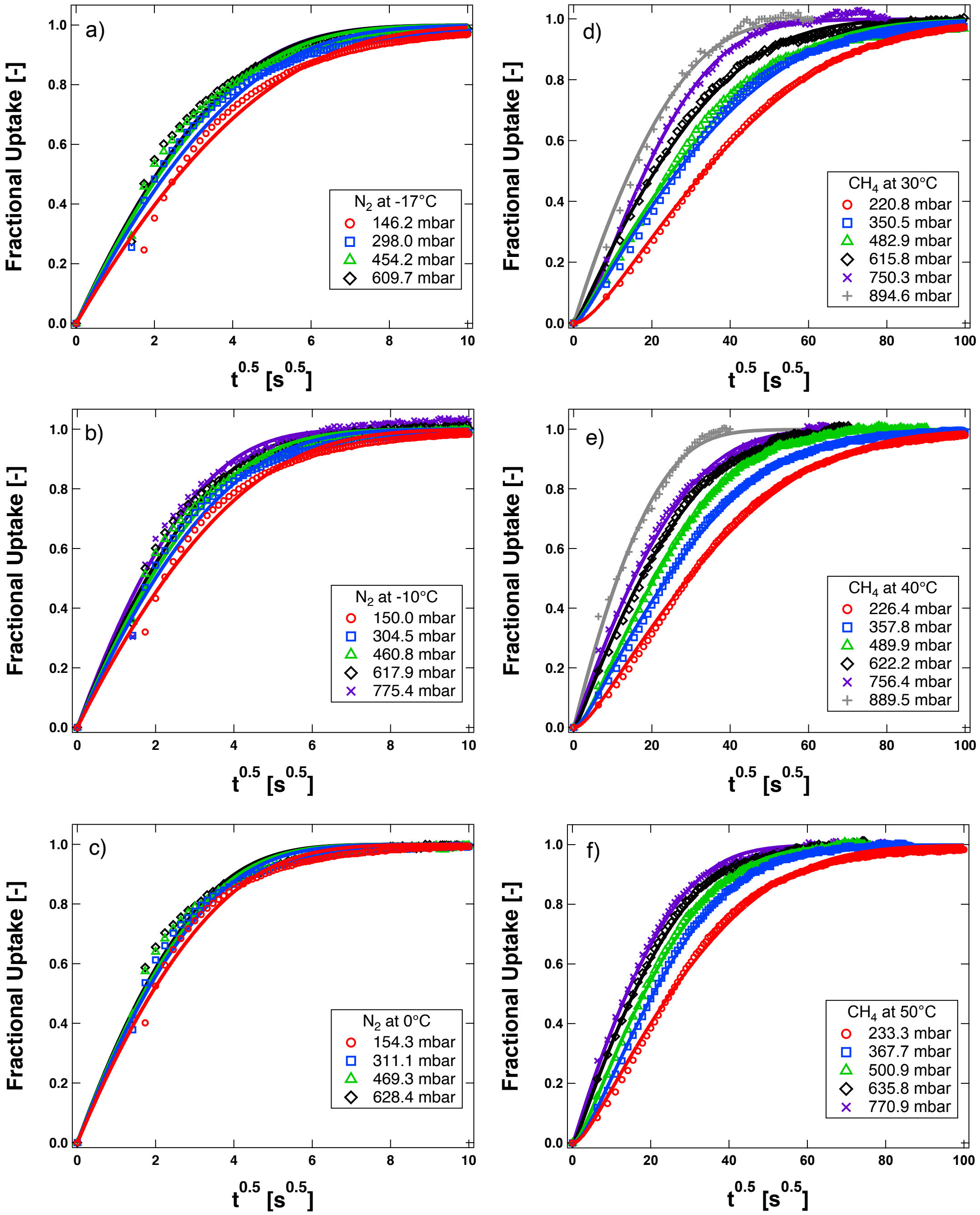

Figure 5: Small dose (constant diffusivity) uptake curves for N_2 at (**a**) -17, (**b**) -10 and (**c**) 0°C and CH_4 at (**d**) 30, (**e**) 40 and (**f**) 50°C on Ba-RPZ crystals. The lines show either the micropore or dual-resistance model fits for N_2 and CH_4, respectively.

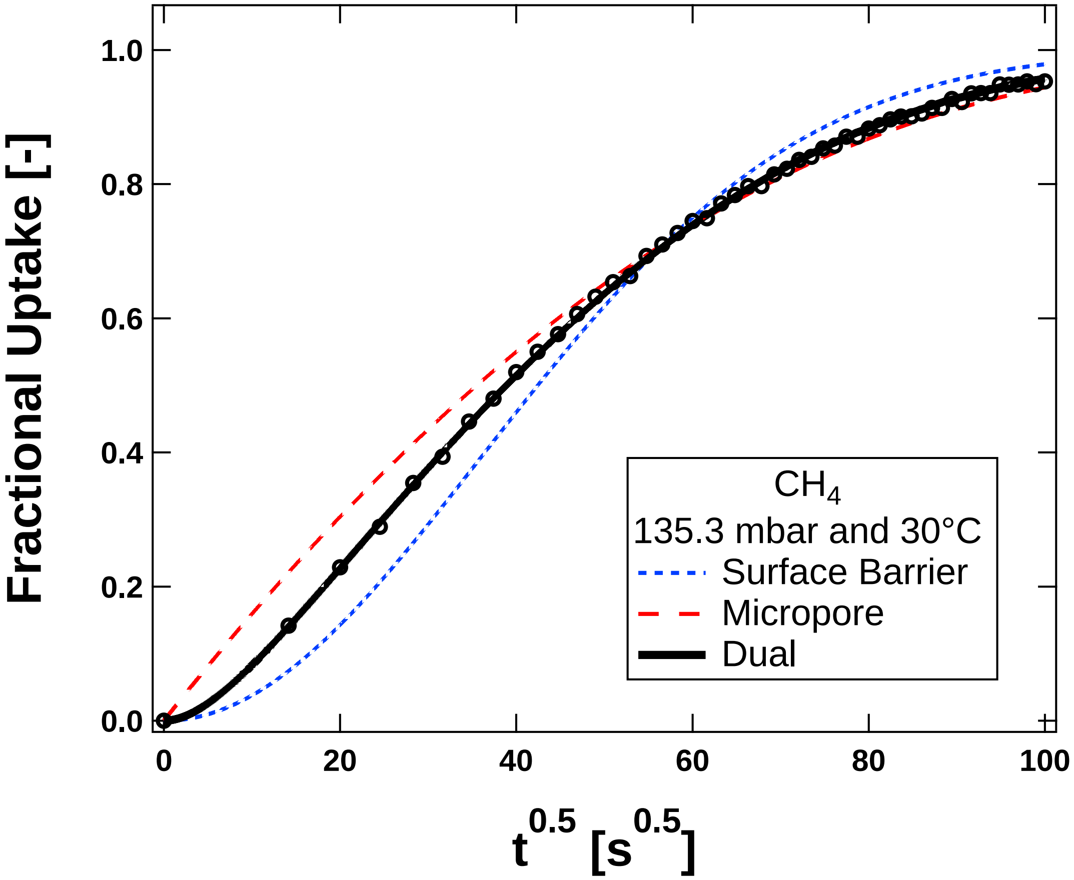

Figure 6: A small dose (constant diffusivity) uptake curve for CH_4 on Ba-RPZ crystals at 135.3 mbar and 30°C. The symbols denote the experimental data while the lines denote fits by various analytical uptake models. Note that every fifth experimental point is plotted to better show the model comparisons.

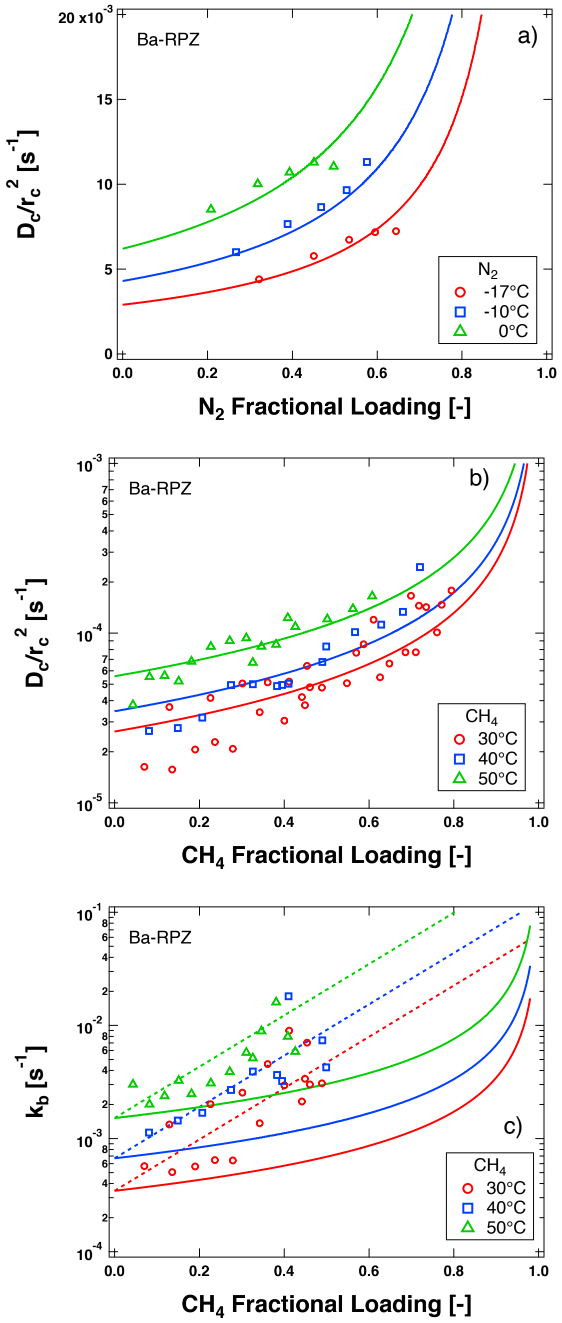

Figure 7: Diffusional constants as a function of solid phase concentration for (**a**) N_2 and (**b**, **c**) CH_4 on Ba-RPZ. The solid lines are Darken predictions and the dashed line is the empirical barrier model prediction.

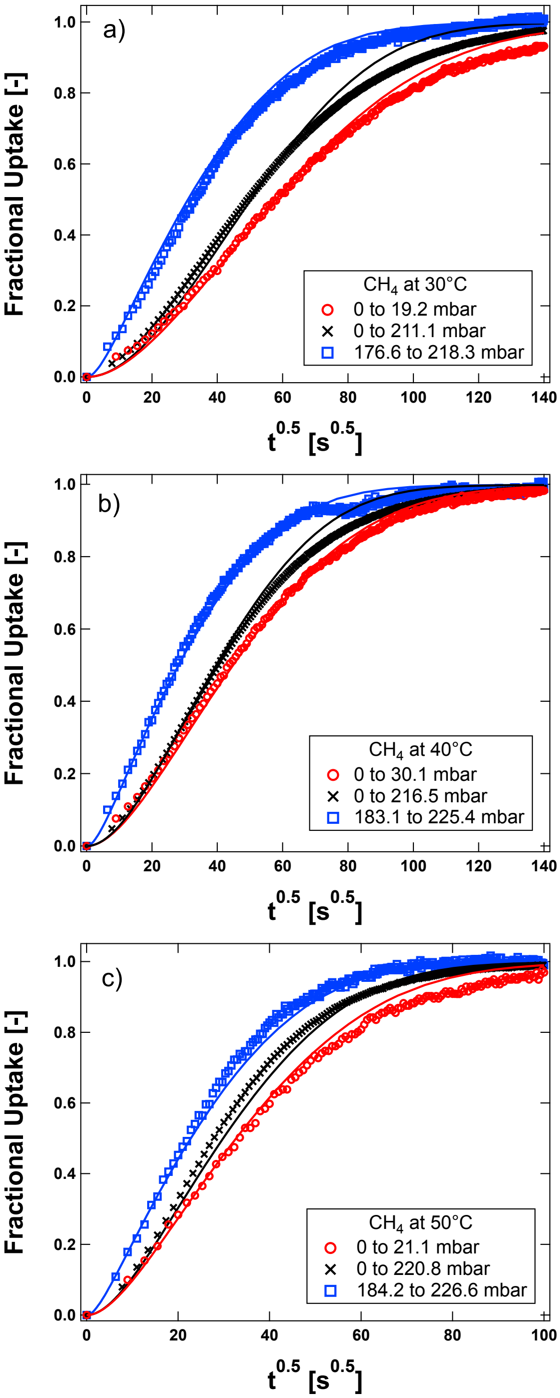

Figure 8: Large dose (non-constant diffusivity) uptake curves for CH_4 on Ba-RPZ crystals at (**a**) 30, (**b**) 40 and (**c**) 50°C. The symbols denote the experimental data while the lines denote the model prediction. Constant diffusivity uptake experiments are shown in red and blue, while large dose experiments are shown in black.

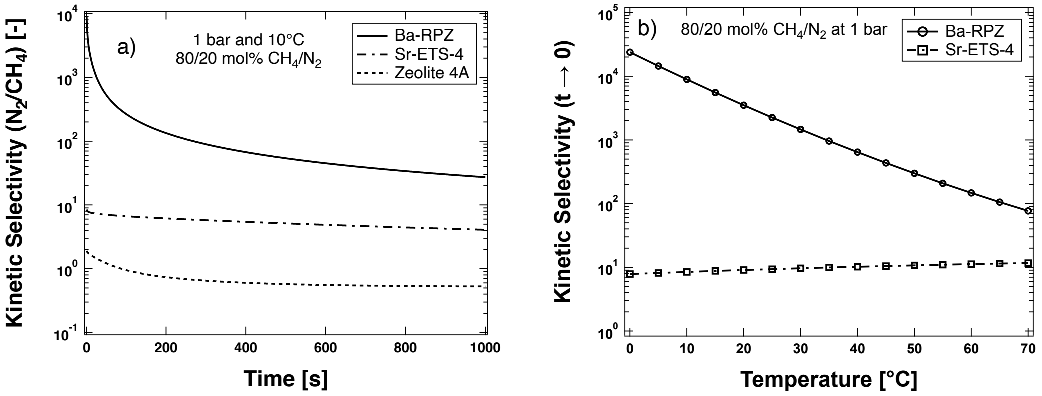

Figure 9: The (**a**) kinetic selectivity for a 80/20 mol% mixture of CH_4/N_2 at 10°C on zeolite 4A, Ba-RPZ and Sr-ETS-4. The (**b**) limiting kinetic selectivity of both Ba-RPZ and Sr-ETS-4 as a function of temperature. Sr-ETS-4 data was calculated from Marathe *et al.*[13].

Table 1: Isotherm parameters for single component N_2 and CH_4 equilibrium on Ba-RPZ and zeolite 4A.

Adsorbent	Gas	Model	$q_\mathrm{b}^\mathrm{sat}$ [mol kg^{-1}]	b_0 [bar^{-1}]	$-\Delta H_\mathrm{ads}$ [kJ mol^{-1}]	K_0 [mol bar^{-1} kg^{-1}]	$-\Delta H_\mathrm{ads}$ [kJ mol^{-1}]
Ba-RPZ	CH_4	SSL	0.8	8.13×10^{-4}	21.06	-	-
	N_2	SSL	0.8	5.26×10^{-5}	25.44	-	-
Zeolite 4A	CH_4	Linear	-	-	-	4.80×10^{-4}	18.38
	N_2	Linear	-	-	-	2.01×10^{-4}	18.89

Table 2: Limiting transport parameters and activation energies for N_2 and CH_4 on Ba-RPZ and zeolite 4A.

Adsorbent	Gas	T [°C]	$D_{c,0}/r_c^2$ [s^{-1}]	$k_{b,0}$ [s^{-1}]	$D'_{c,0}/r_c^2$ [s^{-1}]	$k'_{b,0}$ [s^{-1}]	$E_{a,d}$ [kJ/mol]	$E_{a,b}$ [kJ/mol]	β_b [-]
Zeolite 4A	N_2	-20	$1.90 \times 10^{-3} \pm 8.93 \times 10^{-5}$	-	38.15	-	20.86	-	-
		-10	$2.76 \times 10^{-3} \pm 1.23 \times 10^{-4}$	-					
		0	$3.92 \times 10^{-3} \pm 1.73 \times 10^{-4}$	-					
	CH_4	30	$7.21 \times 10^{-4} \pm 2.34 \times 10^{-5}$	-	6.418	-	22.93	-	-
		40	$9.56 \times 10^{-4} \pm 2.15 \times 10^{-5}$	-					
		50	$1.27 \times 10^{-3} \pm 1.31 \times 10^{-5}$	-					
Ba-RPZ	N_2	-17	$2.09 \times 10^{-3} \pm 3.30 \times 10^{-4}$	-	536.6	-	25.77	-	-
		-10	$4.30 \times 10^{-3} \pm 1.75 \times 10^{-4}$	-					
		0	$6.20 \times 10^{-3} \pm 6.71 \times 10^{-4}$	-					
	CH_4	30	$2.63 \times 10^{-5} \pm 3.30 \times 10^{-6}$	$3.45 \times 10^{-4} \pm 9.37 \times 10^{-5}$	4.498	7.869×10^{6}	30.46	60.19	5.223
		40	$3.46 \times 10^{-5} \pm 8.46 \times 10^{-6}$	$6.69 \times 10^{-4} \pm 1.07 \times 10^{-4}$					
		50	$5.57 \times 10^{-5} \pm 4.45 \times 10^{-6}$	$1.52 \times 10^{-3} \pm 2.68 \times 10^{-4}$					

Table 3: Comparison of limiting diffusivities and activation energies of N_2 and CH_4 on zeolite 4A with literature studies.

Gas	Adsorbent	Temperature Range [°C]	$D_{c,0}/r_c^2$ [s^{-1}]	$E_{a,d}$ [kJ/mol]	Citation
CH_4	Synthesized 4A crystals	0 – 50	1.50×10^{-4}	24.69	Yucel and Ruthven[29]
	Linde 4A pellets	50 – 200	6.06×10^{-4} to 5.92×10^{-3}	18.66	Haq and Ruthven[30]
	UOP 4A pellets	-20 – 10	9.99×10^{-5} to 3.80×10^{-4}	26.78	Cao *et al.*[31]
	UOP 4A pellets	0 – 20	8.90×10^{-4} to 1.80×10^{-3}	21.76	Ahn *et al.*[6]
	Arkema NK10AP Siliporite	30 – 50	7.21×10^{-4} to 1.27×10^{-3}	22.93	present study
N_2	Synthesized 4A crystals	-30 – 50	3.00×10^{-3}	23.43	Yucel and Ruthven[29]
	Linde 4A pellets	25 – 90	2.95×10^{-3} to 1.15×10^{-2}	19.00	Haq and Ruthven[30]
	UOP 4A pellets	-20 – 10	1.50×10^{-3} to 4.50×10^{-3}	22.18	Cao *et al.*[31]
	UOP 4A pellets	0 – 20	8.50×10^{-3} to 2.10×10^{-2}	19.25	Ahn *et al.*[6]
	Arkema NK10AP Siliporite	-20 – 0	1.90×10^{-3} to 3.92×10^{-3}	20.86	present study

For Table of Contents Use Only

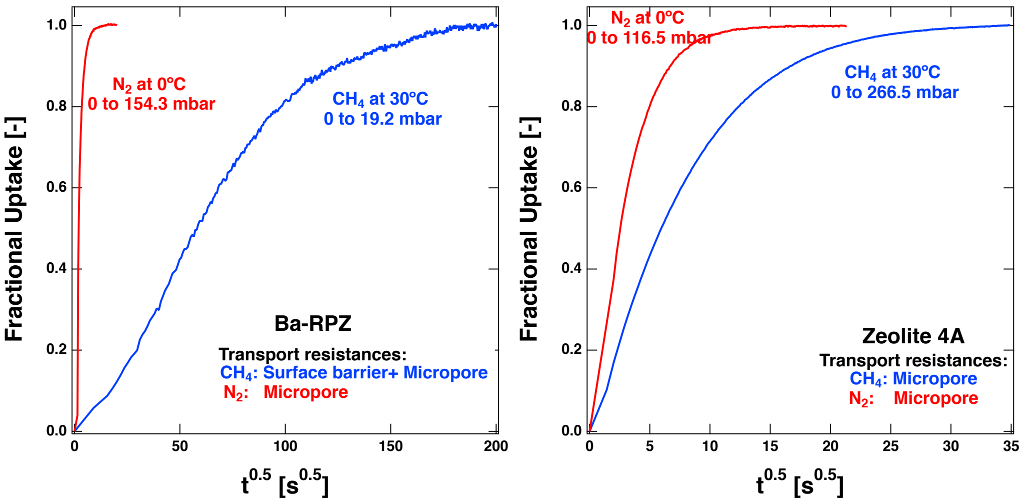

Characteristic uptake curves of CH_4 and N_2 on Ba-RPZ and Zeolite 4A